



## ARTICLE

# Virtual clinical trial simulations for a novel KRAS<sup>G12C</sup> inhibitor (ASP2453) in non-small cell lung cancer

Hiroyuki Sayama<sup>1</sup> | Diana Marcantonio<sup>2</sup> | Takeyuki Nagashima<sup>1</sup> | Masashi Shimazaki<sup>3</sup> |  
Tsuyoshi Minematsu<sup>1</sup> | Joshua F Apgar<sup>2</sup> | John M. Burke<sup>2</sup> | Lucia Wille<sup>2</sup> |  
Yasuhisa Nagasaka<sup>1</sup> | Daniel C. Kirouac<sup>2</sup>

<sup>1</sup>Astellas Pharma Inc, Ibaraki, Japan

<sup>2</sup>Applied BioMath LLC, Concord, Massachusetts, USA

<sup>3</sup>Astellas Research Institute of America LLC, Northbrook, Illinois, USA

## Correspondence

Daniel C. Kirouac, 561 Virginia Road, Suite 220 Concord, MA 01742, USA.  
Email: dkirouac@notchtx.com

Hiroyuki Sayama, 21, Miyukigaoka, Tsukuba-shi, Ibaraki 305-8585, Japan.  
Email: hiroyuki.sayama@astellas.com

## Funding information

This study was funded by Astellas Pharma Inc., Japan.

## Abstract

KRAS is a small GTPase family protein that relays extracellular growth signals to cell nucleus. KRAS<sup>G12C</sup> mutations lead to constitutive proliferation signaling and are prevalent across human cancers. ASP2453 is a novel, highly potent, and selective inhibitor of KRAS<sup>G12C</sup>. Although preclinical data suggested impressive efficacy, it remains unclear whether ASP2453 will show more favorable clinical response compared to more advanced competitors, such as AMG 510. Here, we developed a quantitative systems pharmacology (QSP) model linking KRAS signaling to tumor growth in patients with non-small cell lung cancer. The model was parameterized using in vitro ERK1/2 phosphorylation and in vivo xenograft data for ASP2453. Publicly disclosed clinical data for AMG 510 were used to generate a virtual population, and tumor size changes in response to ASP2453 and AMG 510 were simulated. The QSP model predicted ASP2453 exhibits greater clinical response than AMG 510, supporting potential differentiation and critical thinking for clinical trials.

## Study Highlights

### WHAT IS THE CURRENT KNOWLEDGE ON THE TOPIC?

KRAS<sup>G12C</sup> mutations lead to constitutive proliferation signaling and are prevalent across human cancers. Currently, several KRAS<sup>G12C</sup> inhibitors are in phase I/II clinical testing and demonstrated single agent activity. ASP2453 is a novel inhibitor of KRAS<sup>G12C</sup>.

### WHAT QUESTION DID THIS STUDY ADDRESS?

It remains unclear whether ASP2453 will show more favorable efficacy than its competitors, such as AMG 510. To address this question, we developed a quantitative systems pharmacology (QSP) model linking KRAS signaling to tumor growth to predict and compare expected antitumor response of ASP2453 and AMG 510.

### WHAT DOES THIS STUDY ADD TO OUR KNOWLEDGE?

Virtual clinical trial simulations were conducted using the QSP model. The results suggest ASP2453 will exhibit superior antitumor efficacy in patients, supporting potential differentiation and critical thinking for clinical trials.

This is an open access article under the terms of the Creative Commons Attribution-NonCommercial-NoDerivs License, which permits use and distribution in any medium, provided the original work is properly cited, the use is non-commercial and no modifications or adaptations are made.

© 2021 The Authors. *CPT: Pharmacometrics & Systems Pharmacology* published by Wiley Periodicals LLC on behalf of American Society for Clinical Pharmacology and Therapeutics

## HOW MIGHT THIS CHANGE DRUG DISCOVERY, DEVELOPMENT, AND/OR THERAPEUTICS?

The current study illustrates the successful application of QSP in drug development, enabling a quantitative understanding of complex preclinical data and prediction of clinical response for anticancer agents.

## INTRODUCTION

KRAS is a small GTPase family protein that relays extracellular growth signals (i.e., EGF/EGFR binding) to the cell nucleus through activation of its downstream signaling cascades, such as the mitogen-activated protein kinase (MAPK) and phosphatidylinositol 3-kinase (PI3K). *KRAS*<sup>G12C</sup> mutations stabilize the active (GTP-bound) form of the RAS-GTP/GDP cycling complex, leading to constitutive proliferation and survival signaling. This point mutation is found in ~ 13% of non-small cell lung cancers (NSCLCs), and to lesser extents in pancreatic and colorectal cancers.<sup>1,2</sup> Although KRAS was long deemed an “undruggable” target, this convention was overturned with the discovery of a compound that covalently binds to the G12-mutant cysteine residue, locking in the GDP-bound inactive state.<sup>3,4</sup> Multiple successive compounds bearing the same mechanism-of-action are now in early phase I/II clinical testing, including AMG 510 (Sotorasib, Amgen), MRTX849 (Adagrasib, Mirati), JNJ-74699157/ARS-3248 (Johnson & Johnson/Wellspring Biosciences), and LY3499446 (Eli Lilly).<sup>3,5,6</sup> Amgen was the first to report clinical data<sup>7</sup> followed by Mirati.<sup>8</sup> Both compounds show impressive single agent activity, with overall response rates (ORRs) of ~ 50% in patients with NSCLC, with no dose-limiting toxicities.

ASP2453 is a novel, highly potent, and selective inhibitor of *KRAS*<sup>G12C</sup>. In *in vitro* experiments, ASP2453 almost completely inhibited phosphorylation of ERK1/2 (p-ERK) after a 2-h treatment in NCI-H1373 and MIA PaCa-2 cell lines, resulting in tumor cell growth inhibition. Following single or multiple oral administrations of ASP2453 to NCI-H1373 tumor bearing xenograft mice, KRAS-GTP, p-ERK, and the downstream phosphorylation of S6 (p-S6) in tumor were significantly suppressed. ASP2453 also demonstrated tumor growth inhibition in a dose-dependent manner in NCI-H1373, MIA PaCa-2, and SW1463 xenograft mice. These preclinical findings strongly suggest that ASP2453 could be highly effective in patients with cancer. However, it remains unclear whether ASP2453 will show more favorable clinical outcomes compared to more advanced competitors warranting an advancement of ASP2453 to clinical trials.

Quantitative systems pharmacology (QSP) is a mathematical modeling approach increasingly being applied across all

stages of drug discovery and development.<sup>9,10</sup> QSP models aim to physiologically describe dynamic interactions between biological systems and therapeutics, a means to gain deeper insight into preclinical data and quantitative translation from animals to humans. Moreover, QSP models specifically capture complex biological responses, such as negative feedback mechanisms, which are known to exist within the MAPK pathway and affect drug responsiveness.<sup>11</sup> Due to its mechanistic nature, QSP serves as a powerful tool for hypothesis generation, prediction of clinical outcomes, and decision making throughout drug discovery and development.

In this paper, we developed a QSP model linking RAS-GTP/GDP signaling to tumor growth in NSCLC to address the following research objectives:

1. To quantitatively understand complex pharmacokinetic/pharmacodynamic (PK/PD) relationships in xenograft mice after ASP2453 treatments.
2. To predict clinical antitumor responses of ASP2453 and its most advanced competitor, AMG 510.
3. To inform decision making on an advancement of ASP2453 to clinical trials based on the comparison of expected efficacy in patients.

To this end, virtual clinical trial simulations in patients with NSCLC were conducted for ASP2453 and AMG 510, and predicted ORRs were compared. The workflow for integrating available *in vitro*, *in vivo*, and clinical data within the mechanism-based model is outlined in Figure 1. Overall, this work demonstrated the utility of a QSP approach in translational research. Further potential applications in clinical drug development and limitations of this approach are also discussed.

## METHODS

### Model structure

The model structure and parameters published by Kirouac et al.<sup>12</sup> for *BRAF*<sup>V600E</sup> were taken as a starting point for linking MAPK signaling through tumor growth. In this model, signaling from RTK1 (a putative receptor tyrosine kinase – EGFR) through RAS, RAF, MEK, and ERK through S6 is described using quantitative logic gates, and drug PK and

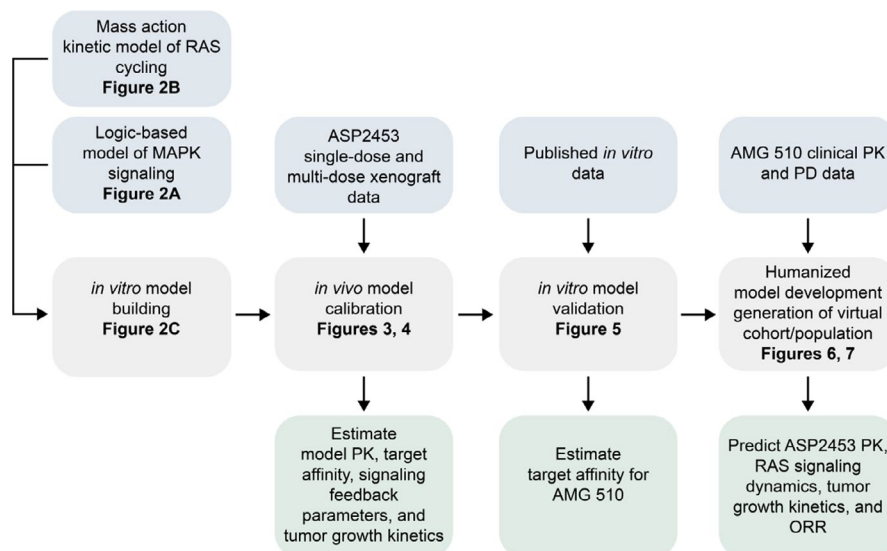


**FIGURE 1** Modelling workflow connecting in vitro, in vivo, and clinical results. The model structure was adapted from two publications covering RAS-GTP cycling and MAPK signal transduction (Figure 2). Calibration was performed using in vivo data from ASP2453-treated xenografts (Figures 3, 4), and in vitro validation and extension using published data on other  $KRAS^{G12C}$ -specific inhibitors AMG 510, MRTX849, ARS-853 and ARS-1620 (Figure 5). Human PK for ASP2453 and AMG 510 was used for clinical translation (Figure 6), and early clinical data on AMG 510 response used to create a virtual population for simulating clinical dose-responses to ASP2453 versus AMG 510 in patients with NSCLC (Figure 7). NSCLC, non-small cell lung cancer; ORR, overall response rate; PD, pharmacodynamic; PK, pharmacokinetic

tumor growth described using ordinary differential equations (ODEs). RAS-mediated PI3K/AKT signaling is also incorporated as a surrogate for MAPK-bypass signaling, integrated by S6. Given the importance of RAS cycling kinetics for this drug class (covalent RAS inhibitors), a mass action kinetics-based model of  $KRAS^{G12C}$  cycling published by Stites and Shaw<sup>13</sup> was integrated as the RAS module, connected to the logic-based signaling modules via regulation of RAF activity.  $KRAS^{G12C}$  mutants signal constitutively, whereas activity of wild-type proteins are regulated by receptor signaling, an effect we accounted for by assuming the maximal rate of signaling by the wild-type is equivalent to the mutant, but the flux is modulated by RTK1. To do so, RTK1 drives the forward rate of wild-type RAS-GDP to RAS-GTP, and the half-maximal effective concentration ( $EC_{50}$ ) of RAF/PI3K activation are set as a fraction of RAS-GTP (mol cell<sup>-1</sup>).

Multiple feedback regulatory circuits operate within the MAPK cascade.<sup>11</sup> The p-ERK induces expression of DUSP, SPRY, and cMYC, which inhibit the phosphorylation and/or expression of ERK, RAS, and RTK1. Crosstalk between PI3K/AKT and MAPK/ERK cascades has also been characterized by an inhibitory interaction from AKT to cRAF, although the mechanism remains unclear.<sup>14,15</sup> These have been implemented via inhibitory species FB1, FB2, FB3, and FB4, respectively, implemented via ODEs downstream of ERK. To enable differing dynamics of the competing feedback processes, transient intermediate species xFB2, xFB3, and xFB4 are

used (DUSP activity is rapid enough that intermediate xFB1 was deemed unnecessary).

The final model structure comprises of 27 species and 75 parameters (Figure 2a,b). Mass-action modules (PKs and RAS-cycling) are coded in units of mol/day, whereas logic-based signal transduction portions are dimensionless, and feedback and tumor growth ODEs are in units of day<sup>-1</sup>.

Pharmacokinetics:

$$\frac{dRASI_{\text{gut}}}{dt} = -k_a \cdot F_a \cdot RASI_{\text{gut}} - k_a \cdot (1 - F_a) \cdot RASI_{\text{gut}}$$

$$\begin{aligned} \frac{dRASI_{\text{blood}}}{dt} = & k_a \cdot F_a \cdot RASI_{\text{gut}} - k_e \cdot RASI_{\text{blood}} \\ & - k_{12} \cdot RASI_{\text{blood}} + k_{21} \cdot \left(\frac{V_1}{V_2}\right) RASI_{\text{tumor}} \\ & - k_p \cdot RASI_{\text{blood}} + k_p \cdot \left(\frac{V_1}{V_p}\right) RASI_{\text{peripheral}} \end{aligned}$$

$$\begin{aligned} \frac{dRASI_{\text{tumor}}}{dt} = & k_{12} \cdot RASI_{\text{blood}} - k_{21} \cdot \left(\frac{V_1}{V_2}\right) RASI_{\text{tumor}} \\ & - \frac{k_{on}}{V_2} \cdot RAS_{\text{mut}}_{\text{GDP}} \cdot RASI_{\text{tumor}} \cdot (1 - f_B) \end{aligned}$$

$$\frac{dRASI_{\text{peripheral}}}{dt} = k_p \cdot RASI_{\text{blood}} - k_p \cdot \left(\frac{V_1}{V_p}\right) RASI_{\text{peripheral}}$$

RAS cycling and drug-mediated inhibition:

$$\frac{dRASwt_{GDP}}{dt} = k_{synth} + (-k_{deg} - k_{fwt} \cdot RTK1) \cdot RASwt_{GDP} + k_{rwt} \cdot RASwt_{GTP}$$

$$\frac{dRASwt_{GTP}}{dt} = (-k_{deg} - k_{rwt}) \cdot RASwt_{GTP} + k_{fwt} \cdot RTK1 \cdot RASwt_{GDP}$$

$$\frac{dRASmut_{GDP}}{dt} = k_{synth} + \left( -k_{deg} - k_{fmut} - \frac{k_{on}}{V_2} \cdot RASi_{tumor} \cdot (1 - f_B) \right) \cdot RASmut_{GDP} + k_{rmut} \cdot RASmut_{GTP}$$

$$\frac{dRASmut_{GTP}}{dt} = (-k_{deg} - k_{rmut}) \cdot RASmut_{GTP} + k_{fmut} \cdot RASmut_{GDP}$$

$$\frac{dRASmut_{GDP}I}{dt} = -k_{deg} \cdot RASmut_{GDP}I + \frac{k_{on}}{V_2} \cdot RASmut_{GDP} \cdot RASi_{tumor} \cdot (1 - f_B)$$

Wherein:

$$k_{synth} = RAS_{SS} \cdot k_{deg} \cdot V_2$$

Signal propagation through MAPK and PI3K pathways:

$$RTK1 = RTK1_b + (RTK1_t - RTK1_b) \cdot \left( 1 - G_{13} \cdot \frac{FB3^{k_{FB3}}}{FB3^{k_{FB3}} + \tau FB3^{k_{FB3}}} \right)$$

$$RAF = RAF_b + (RAF_t - RAF_b) \cdot \left( \frac{RAS^{k_2}}{RAS^{k_2} + \tau 2^{k_2}} \right) \cdot \left( 1 - G_{SPRY} \cdot \frac{FB2^{k_{FB2}}}{FB2^{k_{FB2}} + \tau FB2^{k_{FB2}}} \right) \cdot \left( 1 - G_4 \cdot \frac{FB4^{k_{FB4}}}{FB4^{k_{FB4}} + \tau FB4^{k_{FB4}}} \right)$$

$$MEK = MEK_b + (MEK_t - MEK_b) \cdot \left( \frac{RAF^{k_3}}{RAF^{k_3} + \tau 3^{k_3}} \right)$$

$$ERK = ERK_b + (ERK_t - ERK_b) \cdot \left( \frac{MEK^{k_4}}{MEK^{k_4} + \tau 4^{k_4}} \right) \cdot \left( 1 - G_{DUSP} \cdot \frac{FB1^{k_{FB1}}}{FB1^{k_{FB1}} + \tau FB1^{k_{FB1}}} \right)$$

$$S6 = S6_b + (S6_t - S6_b) \cdot \left( \frac{(w_{OR} \cdot ERK + (1 - w_{OR}) \cdot AKT)^{k_6}}{(w_{OR} \cdot ERK + (1 - w_{OR}) \cdot AKT)^{k_6} + \tau 6^{k_6}} \right)$$

$$PI3K = PI3K_b + (PI3K_t - PI3K_b) \cdot \left( \frac{w_{RAS} \cdot RAS^{k_7}}{w_{RAS} \cdot RAS^{k_7} + \tau 7^{k_7}} \right)$$

$$AKT = AKT_b + (AKT_t - AKT_b) \cdot \left( \frac{PI3K^{k_8}}{PI3K^{k_8} + \tau 8^{k_8}} \right)$$

Wherein:

$$RAS = \frac{RASmut_{GTP} + RASwt_{GTP}}{V_2}$$

Feedback regulatory circuits:

$$\frac{dFB1}{dt} = r_1 \cdot ERK - deg_1 \cdot FB1$$

$$\frac{dxFB2}{dt} = r_2 \cdot ERK - deg_2 \cdot xFB2$$

$$\frac{dxFB3}{dt} = r_3 \cdot ERK - deg_3 \cdot xFB3$$

$$\frac{dxFB4}{dt} = r_4 \cdot PI3K - deg_4 \cdot xFB4$$

$$\frac{dFB2}{dt} = deg_2 \cdot xFB2 - deg_2 \cdot FB2$$

$$\frac{dFB3}{dt} = deg_3 \cdot xFB3 - deg_3 \cdot FB3$$

$$\frac{dFB4}{dt} = deg_4 \cdot xFB4 - deg_4 \cdot FB4$$

Tumor growth regulation:

$$\frac{dTD}{dt} = r_5 \cdot (S6 - TD)$$

$$\frac{dCells}{dt} = \left( \mu_{MAX} \cdot \left( \frac{TD^{k_g}}{TD^{k_g} + \tau g^{k_g}} \right) - \delta_{MAX} \right) \cdot Cells \cdot \left( 1 - \frac{Cells}{V_{MAX}} \right)$$

## Parameter estimation

The logic-based model of MAPK signaling<sup>12</sup> reported 20 parameter sets, which equivalently described the in vitro and in vivo data. This model was, however, developed in the context of *BRAF*<sup>V600E</sup>-driven tumors. *BRAF* species and associated reactions and parameters were thus deleted, as *KRAS* predominantly signals through cRAF. Parameters for the mass action kinetics-based RAS cycling module were taken from literature reported values (Table 1).

PK parameters of ASP2453 for xenograft-bearing mice and humans were estimated from preclinical experimental data and predicted human PK profile, respectively, by

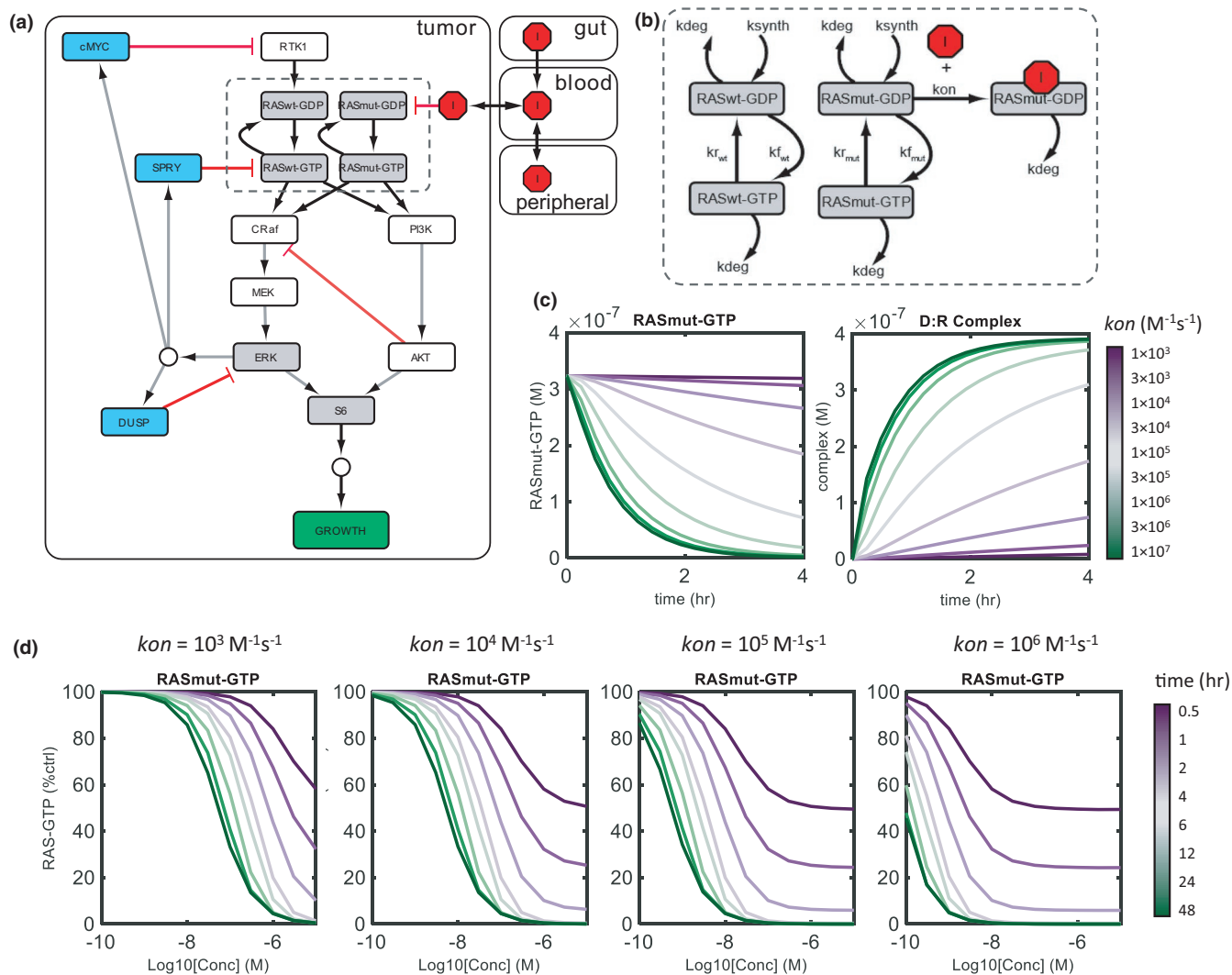


**FIGURE 2** Model structure and dynamics in response to *KRAS*<sup>G12C</sup> inhibitor treatment. (a) The logic-based model of MAPK signaling developed in the context of *BRAF*<sup>V600E</sup> mutations<sup>12</sup> was modified to account incorporate *KRAS*<sup>G12C</sup> activating mutations. (b) Mass-action kinetics-based model of RAS cycling<sup>13</sup> was integrated to account for kinetics of KRAS-inhibitor binding, linking receptor activation (RTK1) to cRAF. (c) RAS-GTP dynamics were simulated in response to a 10 nM dose of inhibitor, with  $k_{on}$  varied from  $10^3$  to  $10^7$  M<sup>-1</sup> s<sup>-1</sup>. Drug-bound RAS reached steady-state for high affinity variants within 2 h, consistent with a RAS-GDP → GTP cycling half-life of ~30 min.<sup>13,21</sup> The dynamics of GDP/GTP cycling affect measured dose response profiles. (d) Treatment with a putative KRAS inhibitors with  $k_{on}$  of  $10^3$ ,  $10^4$ ,  $10^5$  and  $10^6$  M<sup>-1</sup> s<sup>-1</sup>, and simulated in vitro RAS-GTP dose-responses at 30 min through 48 h

**TABLE 1** RAS mass action kinetics parameters

Parameter	Value	Unit	References
[KRAS]	$1 \times 10^6$	Molecules/cell	Mageean et al. (2015) <sup>31</sup> ; Sunaga et al. (2011) <sup>32</sup>
[KRAS]	$5 \times 10^{-7}$	M	Assuming average cell volume of 4 pL
KRAS half-life	24	Hours	Shukla et al. (2014) <sup>33</sup>
GTP → GDP half-life	30	Minutes	Patricelli et al. (2016) <sup>34</sup>
% KRAS-GTP at steady state	80	%	Patricelli et al. (2016) <sup>34</sup>

minimizing mean squared error of log<sub>10</sub>-data using Particle Swarm Optimization (PSO) with 40 particles and 100 iterations, using the default settings of MATLAB *particleswarm* function. PK parameters of AMG 510 in humans were

estimated from digitized clinical data in the same manner. Parameters specifying the mass-action module (PK and  $k_{on}$ ) were found to converge to unique values. Cell signaling feedback and tumor growth parameters were similarly estimated

from in vivo xenograft data using PSO with 100 particles and 500 iterations. For these, PSO was run 20 times, once for each of the stating 20 parameter sets specifying the logic-based signaling module (Table S1). Many of these parameters are nonidentifiable, although no systematic analysis was performed. All PD simulations represent an average of the results from the 20 parameter sets.

## Virtual population generation

For model translation, we first estimated AMG 510 human PK parameters based on data from Amgen presentation at ESMO 2019.<sup>7</sup> Binding affinity of AMG 510 was estimated from published in vitro data ( $k_{on} = 1.2 \times 10^4 \text{ M}^{-1} \text{ s}^{-1}$ ),<sup>16</sup> and protein bound-fraction was assumed to be the same as that measured for ASP2453 ( $f_b = 0.9926$ ). All intracellular signaling parameters were assumed to be conserved between the xenograft and human tumors. Two parameters that were chosen for scaling were the rates of tumor cell proliferation ( $\mu_{max}$ ) and cell death ( $\delta_{max}$ ). Although other model parameters (i.e., RTK1 expression level: *RTK1t*) are likely to vary between species, and between individual patients, cell proliferation and death rates are both known to vary and are highly sensitive.

A virtual cohort of 1000 subjects (i.e., parameter sets) was generated by first random resampling from the 20 parameter sets comprising the mouse model. The parameters  $\mu_{max}$  and  $\delta_{max}$  were scaled to 0.1 and 0.2 times the values estimated from the mouse model and randomized by sampling from a log normal distribution with mean of the scaled value, and standard deviation of 0.02. Simulations of tumor size change at 6 weeks for the virtual cohort are shown in Figure S1.

The virtual cohort was used to generate a virtual population consistent with the clinical data. That is:

1. Control tumor growth varying from approximately one to threefold from baseline at 6 weeks, based on published meta-analysis of NSCLC tumor volume doubling times.<sup>17</sup>
2. Distribution of tumor size changes after 6 weeks treatment with AMG 510 at 180–960 mg from the waterfall plot presented by Amgen at ESMO (digitized in Table S2).

A prevalence weight (PW) was calculated for each parameter set (i.e., subjects) in the virtual cohort. This was done by:

1. Applying a  $PW = 0$  (exclusion) for each parameter set that resulted in less than 0.9 OR greater than 3-fold change in tumor size at 6 weeks for control treatment.

2. Categorize the AMG 510 waterfall plot data into 20% bins ranging from 0–20% to 100–120% change from baseline. Simulated tumor size changes for the virtual cohort were then categorized by bin, and PW computed as:

$$PW_i = f_{data_i} / f_{vc_i}$$

Wherein PW for virtual subjects in bin  $i$  ( $PW_i$ ) is based on the frequency of clinical data in bin  $i$  ( $f_{data_i}$ ) and the frequency of virtual cohorts in bin  $i$  ( $f_{vc_i}$ ). The PW vector was then scaled to 1.

Resampling 200 parameter sets from the virtual cohort with frequency specified by the PW then produced the virtual population consistent with the clinical data. All subsequent clinical simulations (ASP2453 vs. AMG 510 dose-responses) were performed by sampling 200 parameter sets specified in the virtual population. The approach is adapted from previous papers.<sup>18,19</sup> The workflow was completed with larger virtual cohorts ( $n = 10,000$ ) to reduce instances of patient resampling, but results were unaffected.

The model was coded in SimBiology, and all simulations and analyses performed in MATLAB R2019b (Mathworks, Natick, MA). Typical model scripts are provided as Supplementary Material. Note these may not be future-compatible with MATLAB releases other than R2019b.

Experimental methods for in vitro p-ERK inhibition, plasma protein binding, in vivo xenograft studies, and human PK prediction are shown in Supplementary Material. All data related to ASP2453 was generated in-house, and data related to alternate compounds (AMG 510, MRTX849, ARS-853, and ARS-1620) were extracted from published literature.

## RESULTS

### Model construction

The model structure was compiled from two separate publications. As a starting point, the model published by Kirouac et al.<sup>12</sup> linking cell signaling through the MAPK cascade to tumor growth was implemented. However, this model was developed in the context of colorectal  $BRAF^{V600E}$  oncogenic driver, rather than  $KRAS^{G12C}$ . To adapt the model to  $KRAS^{G12C}$  NSCLC, we integrated a mass action kinetics-based module developed by Stites and Shaw,<sup>13</sup> describing cycling of RAS-GDP to RAS-GTP isoforms in place of the original logic-based equations, and removed the  $BRAF^{V600E}$  species and associated reactions (Figure 2a,b). RAS inhibition by covalent modification was implemented as a unidirectional reaction between compound and RAS-GDP, characterized by the target association rate ( $k_{on}$ ). This is a summation of  $k_{inact}/K_i$ , typically used to describe the efficiency of covalent

bond formation resulting from the potency ( $K_i$ ) of the first reversible binding event and the maximum potential rate ( $k_{\text{inact}}$ ) of inactivation.<sup>20</sup> The 20 previously published parameter sets that equivalently described response to BRAF, MEK, and ERK inhibitors in *BRAF*<sup>V600E</sup> tumor cell lines were found to qualitatively capture dose-responses to a putative KRAS inhibitor (Figure S2).

### Simulations of in vitro RAS-GTP dynamic response to inhibitor treatment

Dynamics of RAS-GTP inhibition in response to a putative RAS inhibitor with varying target affinities

were simulated. Implementing a GTP-GDP half-life of 30 min resulting in the system reaching steady-state by ~ 2 h when treated with a potent inhibitor (Figure 2c), consistent with published target engagement kinetics.<sup>13,21</sup> All other parameters were taken directly from the published model.<sup>12</sup> For high affinity/high dose treatment, the kinetics of RAS-GTP inhibition is limited by the RAS-GTP/GDP cycling rate rather than target engagement kinetics. As a result, dose-response curves for RAS-GTP inhibition display time-dependence. That is, the apparent  $EC_{50}$  shifts toward increased potency as assay time increases, plateauing at 24–48 h (Figure 2d), consistent with published data for this class of compounds.<sup>16,22</sup>

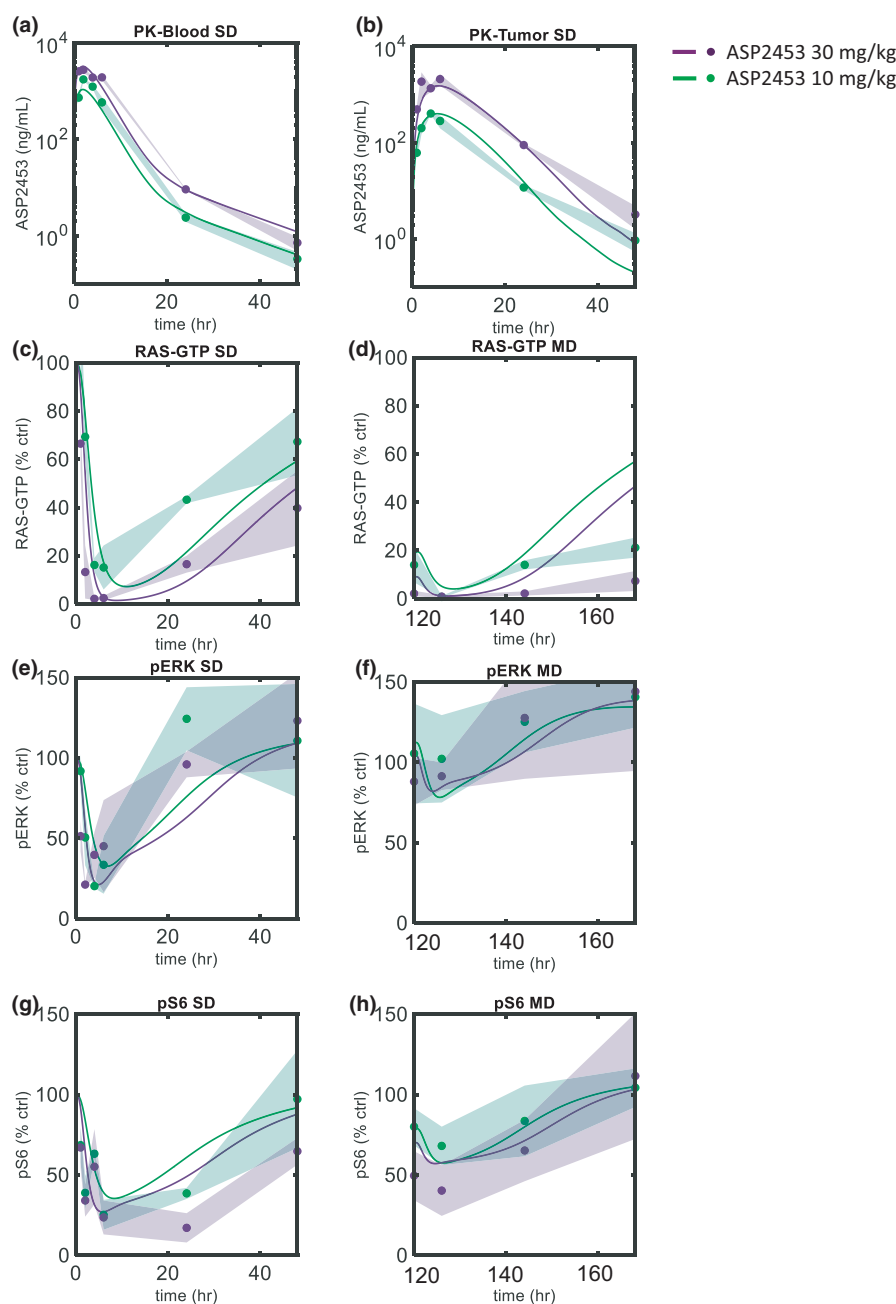


**FIGURE 3** Model fitting to ASP2453 in vivo pharmacokinetic (PK) and pharmacodynamic (PD) data. A three-compartment PK model comprising central, peripheral, and tumor compartments was fit to plasma (a) and tumor (b) PK time-course data. Simulated in vivo KRAS-GTP dynamics following single (SD: c) and multiple doses (5 days q.d., MD: d) of ASP2453, and overlaid with data (mean, and  $\pm$  standard deviation represented as shaded areas). Simulated p-ERK (e, f) and p-S6 (g, h) PD profiles following single (SD) and multiple doses (MDs) of ASP2453 (an average of the results from the 20 parameter sets), overlaid with experimental data (mean  $\pm$  standard deviation)

## Modeling of PK/PD and tumor growth profiles in murine xenografts

Given that the model structure adequately describes both RAS-GTP/GDP kinetics and cellular signal transduction, we used *in vivo* data from xenograft studies to successively estimate model PK, target affinity, and signaling feedback parameters. First, a three-compartment PK model was fit to plasma and tumor concentration time-course data following 10 and 30 mg kg<sup>-1</sup> dosing of ASP2453 in NCI-H1373 xenograft-bearing mice (Figure 3a,b, Table 2).

Tumor KRAS-GTP dynamics over 48 h following single dose (SD; Figure 3c), and 5-day q.d. dosing (multiple dose [MD]; Figure 3d) were quantified via GTP-pull down assays on tumor lysate. To estimate  $k_{on}$  of ASP2453, the PK model

and measured protein bound fraction ( $f_b = 0.996$ ) was used to simulate tumor KRAS-GTP dynamics.  $k_{on}$  for ASP2453 was estimated to be  $5 \times 10^5 \text{ M}^{-1} \text{ s}^{-1}$  by fitting the single dose RAS-GTP PD simulations to the experimental data. However, after MDs, experimentally measured KRAS-GTP is suppressed to a greater extent than predicted by the model, a phenomenon that cannot be explained by tumor accumulation of free drug.

The PD profiles of the downstream signaling readouts p-ERK and p-S6 were found to change after repeat dosing (Figure 3e–h). Following 5 days of q.d. treatment with ASP2453, both p-ERK and p-S6 are much less sensitive to KRAS-GTP inhibition (i.e., the maximum % inhibition decreases), a phenomenon reported previously for MRTX849.<sup>22</sup> The p-ERK in fact rebounds above baseline value by 24 h post-treatment. This is likely due to the activation of multiple feedback circuits regulated by ERK,<sup>11</sup> implemented in the model as mediated by DUSP, SPRY, and cMYC, as well as via pathway cross talk from AKT to cRAF.<sup>14,15</sup> The PD profiles of p-ERK and p-S6 were used to estimate 25 parameters defining signaling and feedback circuits across all 20 parameter sets from the original BRAF/MAPK model (Table S1). The resulting model simulations are consistent with the data, capturing the loss of signaling responsiveness following MDs (Figure 3e–h). Full 15-day dynamic simulations are shown in Figure S3.

NCI-H1373 tumor xenograft-bearing mice were treated with ASP2453 at a dose range of 1.25 to 30 mg kg<sup>-1</sup> q.d., and tumor size was measured over 15 days. These data were used to estimate six model parameters connecting p-S6 activation to tumor growth (Table S1). The fitted model is consistent with data, showing dose-dependent reduction in tumor growth, with tumor stasis achieved at ~ 10 mg kg<sup>-1</sup> q.d. (Figure 4a).

**TABLE 2** PK parameters for ASP2453 and AMG 510

Parameter	ASP2453 (mouse)	ASP2453 (human)	AMG 510 (human)
$k_a$ (1/day)	15.88	23.4	58.1
$V_1$ (L) <sup>a</sup>	0.0834	1309	110
$V_p$ (L) <sup>a</sup>	0.010	330.4	4.40
$k_p$ (1/day)	0.235	0.497	0.0908
$k_e$ (1/day)	9.98	1.91	2.98
$k_{12}$ (1/day)	0.0059	0.0059 <sup>b</sup>	0.0059 <sup>b</sup>
$k_{21}$ (1/day)	0.0051	0.0051 <sup>b</sup>	0.0051 <sup>b</sup>
$k_{on}$ (M <sup>-1</sup> s <sup>-1</sup> )	5E+05	5E+05 <sup>b</sup>	12,000
$f_b$	0.996	0.9926	0.9926 <sup>c</sup>

<sup>a</sup>Assume 20 g body weight mouse, 70 kg human.

<sup>b</sup>Assume same as ASP2453 xenograft values.

<sup>c</sup>Assume same as ASP2453 human value.

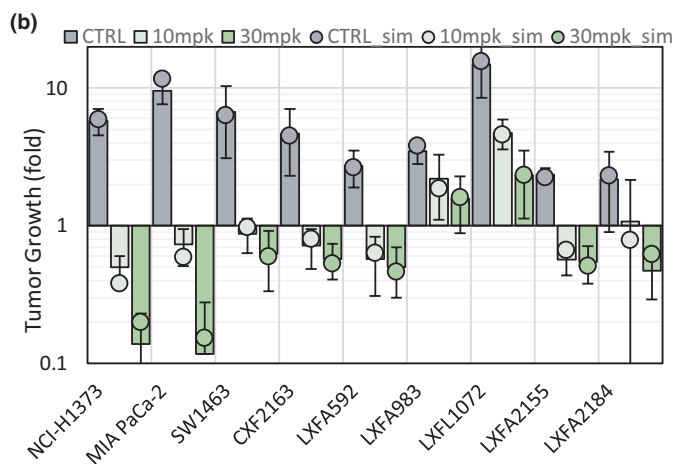
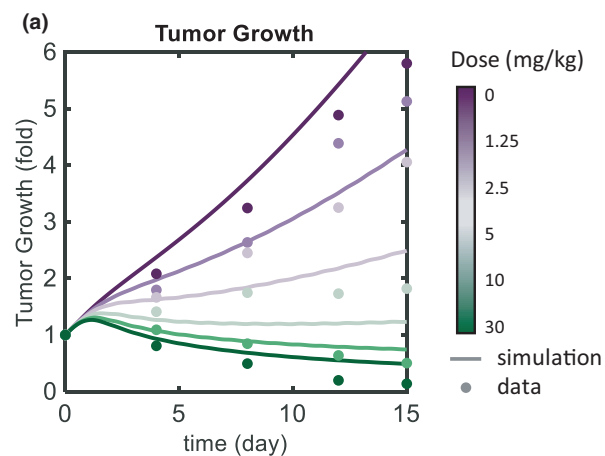


**FIGURE 4** *In vivo* tumor xenograft model fitting. (a) NCI-H1373 xenograft kinetics in response to QD dosing of ASP2453 at 0 (ctrl), 1.25, 2.5, 5, 10, and 30 mg kg<sup>-1</sup> (an average of the results from the 20 parameter sets). (b) Tumor growth at 15 days for nine cell line- and patient-derived xenografts treated with 0 (ctrl), 10 and 30 mg kg<sup>-1</sup> ASP2453 q.d. Error bars represent  $\pm$  standard deviation of the observed data

To ensure results were not unique to NCI-H1373 xenografts, eight additional *KRAS*<sup>G12C</sup> cell line- and patient-derived xenograft tumor models were treated with 10 and 30 mg kg<sup>-1</sup> ASP2453 (q.d.), and tumor sizes measured over 15 days. Dose-dependent antitumor activity of ASP2453 was observed in all models, whereas the baseline tumor growth and sensitivity varied (Figure 4b). Model simulations accurately captured the observed activity in each xenograft by adjusting only two parameters –  $\mu_{\max}$  and  $\delta_{\max}$  (Figure S4), keeping all other parameters consistent. Although other physiological parameters (i.e., protein expression levels) are likely to vary between xenografts and individual patients, these two are sufficient to account for the observed diversity in tumor responses, and may be minimally sufficient to capture interindividual variability for clinical projections.

Local parameter sensitivity analysis identified additional combination targets consistent with findings from other

*KRAS* inhibitors<sup>16,22,23</sup> (Figure S5a), and additional simulations predicted *in vivo* combination effect reported for the compound MRTX849<sup>22</sup> (Figure S5b).

## Model validation using *in vitro* data and expansion to AMG 510

NCI-H1373 cells were grown in culture, treated with dose-range of ASP2453, and p-ERK was quantified 2 h post-treatment via enzyme-linked immunosorbent assay (ELISA). Using the *in vivo* parameterized model, simulations of both *KRAS*-GTP and p-ERK, recapitulating the experimental protocol, were overlaid with the observed data (Figure 5a). The simulated p-ERK dose-response quantitatively matches the experimental results. To assess sensitivity of results to the estimated  $k_{\text{on}}$ , simulations were performed varying affinity. Setting bounds at  $\pm$  twofold the *in vivo* estimated value ( $k_{\text{on}} = 2.5\text{--}10 \times 10^5 \text{ M}^{-1} \text{ s}^{-1}$ ) fully

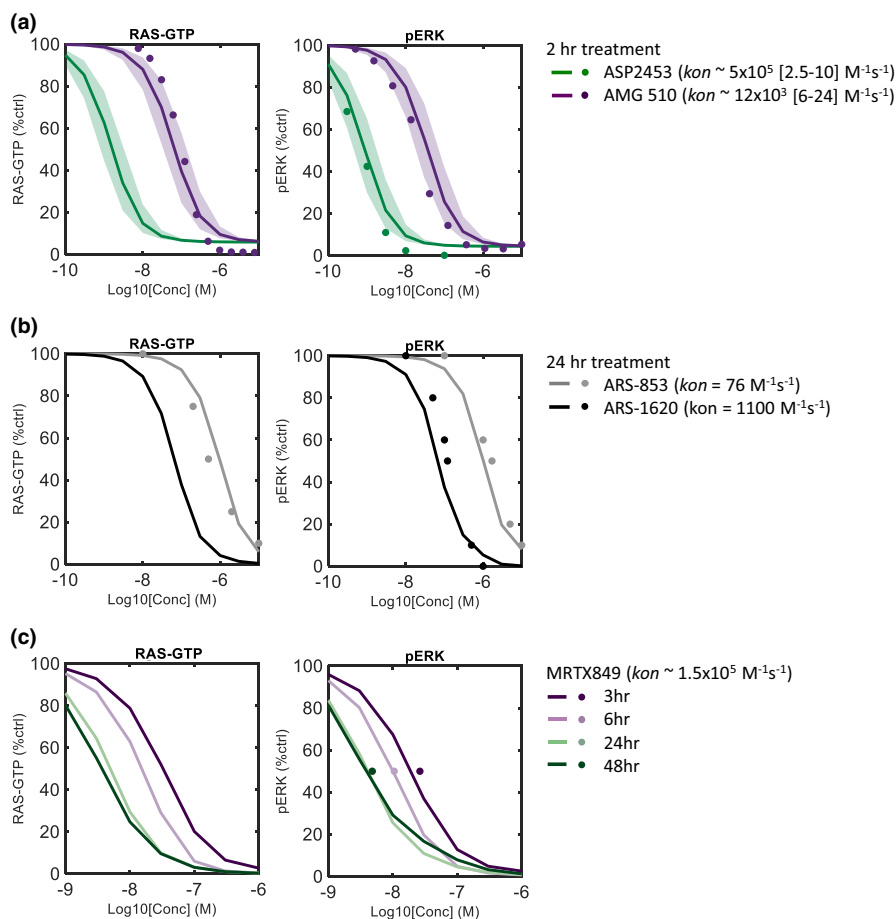


**FIGURE 5** *In vitro* model validation using ASP2453, ARS-853, ARS-1620, AMG 510, and MRTX849 dose-response data. (a) Published RAS-GTP and p-ERK dose-responses to AMG 510<sup>16</sup> (2 h treatment) were overlaid with simulated curves with a  $k_{\text{on}}$  estimate of  $12 \times 10^3 \text{ M}^{-1} \text{ s}^{-1}$ , consistent with the reported value of  $9.9 \pm 1.8 \times 10^3 \text{ M}^{-1} \text{ s}^{-1}$ . Similarly, experimentally measured p-ERK dose-responses to ASP2453 treatment (2 h) overlaid with model simulations with  $k_{\text{on}}$  of  $5 \times 10^5 \text{ M}^{-1} \text{ s}^{-1}$ . Shaded areas represent  $\pm$  2-fold estimated affinity. (b) 24-h treatment simulations with ARS-853 and ARS-1620 implemented using reported  $k_{\text{on}}$  of 76 and  $1100 \text{ M}^{-1} \text{ s}^{-1}$ , respectively, and overlaid with published simulations<sup>13</sup> and experimental data.<sup>21</sup> (c) MRTX849 reported time-dependent p-ERK half-maximal effective concentration ( $\text{EC}_{50}$ ) values<sup>22</sup> were overlaid on simulated dose-response curves at 3, 6, 24, and 48 h with a  $k_{\text{on}}$  estimated at  $1.5 \times 10^5 \text{ M}^{-1} \text{ s}^{-1}$

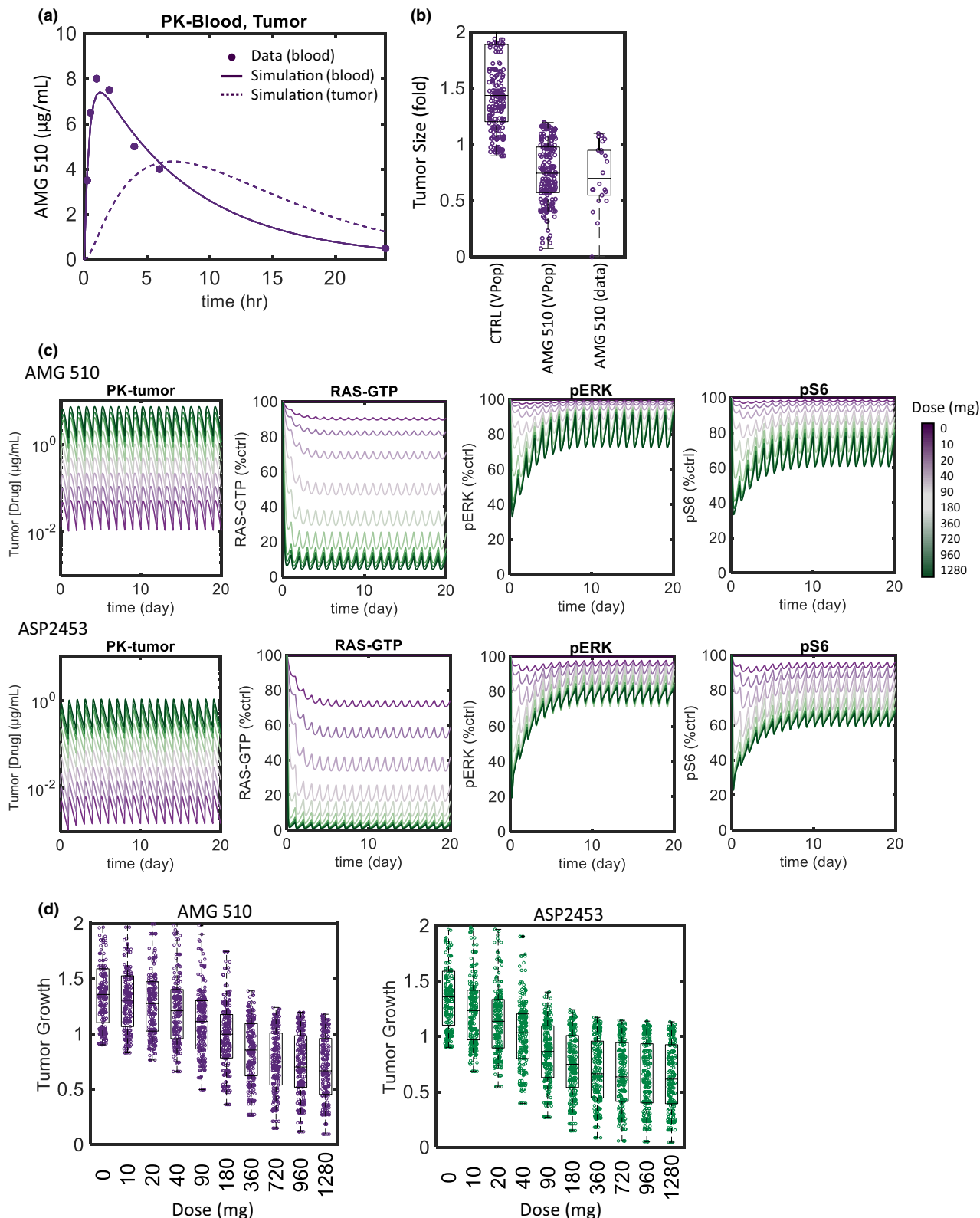


**FIGURE 6** Clinical translation using virtual populations. (a) Published AMG 510 clinical pharmacokinetic (PK) data (960 mg<sup>7</sup>) was digitized and fit using a two-compartment model. Tumor PK profiles were estimated based on tumor penetrating coefficients estimated for ASP2453. Digitized data represented as dots, simulated plasma PK as solid line, and predicted tumor PK as dashed line. (b) Published tumor response data for 22 NSCLC patients treated with AMG 510 at 6 weeks was digitized and used to derive a virtual population.<sup>7</sup> (c) Model simulations of tumor drug concentration, RAS-GTP, p-ERK, and p-S6 dynamics over 20 days in response to q.d. treatment with AMG 510 versus ASP2453 at 10 through 1280 mg (an average of the results from the 200 virtual population for p-ERK/p-S6). (d) Model simulated tumor size changes at 6 weeks for 200 virtual patients treated with AMG 510 versus ASP2453

captured the p-ERK dose-response curve. To directly compare in vitro potency of ASP2453 to AMG 510, we used published in vitro dose-response data for AMG 510.<sup>16</sup> KRAS-GTP measurements were attained in a nucleotide-exchange assay with recombinant KRAS (G12C/C118A), and p-ERK dose response data from the same experimental protocol as ASP2453, although using two alternate *KRAS*<sup>G12C</sup>-mutant cancer cell lines (NCI-H358 and MIA PaCa-2). By matching model simulations to the experimental data, we estimate  $k_{on}$  of AMG 510 to be  $\sim 12 \times 10^3 \text{ M}^{-1} \text{ s}^{-1}$  (Figure 5a), with a twofold spread in this value ( $6\text{--}24 \times 10^3 \text{ M}^{-1} \text{ s}^{-1}$ ) fully capturing the curves. This is within bounds of the reported value of  $k_{inact}/K_i$  (equivalent to  $k_{on}$ ) for AMG 510, measured via mass spectrometry as  $9.9 \pm 1.8 \times 10^3 \text{ M}^{-1} \text{ s}^{-1}$ ,<sup>16</sup> or  $\sim 50$ -fold lower than estimated for ASP2453.

To further validate model predictions in vitro, we utilized published dose-response data for other *KRAS*<sup>G12C</sup>-specific inhibitors with the same mechanism of action. First, we simulated KRAS-GTP and p-ERK dose-response curves after 24-h treatment with the tool compounds ARS-853 and ARS-1620, based on reported  $k_{inact}/K_i$  ( $k_{on}$ ) values of 76 and  $1100 \text{ M}^{-1} \text{ s}^{-1}$ .<sup>13,21</sup> Data from the Figure S3 of ref. 21 was digitized and overlaid on the simulated curves (Figure 5b). Model predicted dose-response curves are similar to published data, without any parameter tuning.

The compound MRTX849 was reported to display time-dependent p-ERK  $EC_{50}$  values,<sup>22</sup> consistent with theoretical model simulations of KRAS-GTP shown in Figure 2d. Estimating the  $k_{on}$  for MRTX849 as  $1.5 \times 10^5 \text{ M}^{-1} \text{ s}^{-1}$ , model simulations replicated the reported time-dependent shift in  $EC_{50}$  values, stabilizing after 24 h (Figure 5c).

In summary, the model quantitatively links binding affinity of covalent inhibitors for RAS-GDP, via RAS-GTP signaling through the MAPK pathway, to p-ERK dose response relationships for multiple compounds, consistent with both published and internal data.

## Clinical translation and virtual population generation

To use the model for clinical predictions, we utilized published AMG 510 clinical data. First, a human PK model for AMG 510 was developed using population average PK time-course data following a single dose of 960 mg.<sup>7</sup> Parameters for a standard two-compartment model were estimated by fitting the digitized data (Table 2). Tumor penetration rates ( $k_{12}$  and  $k_{21}$ ) were assumed to be the same as estimated for ASP2453 xenografts, and tumor PK projections from such overlaid on the fitted model (Figure 6a).

Published tumor-size change data (waterfall plot) at 6 weeks following q.d. dosing of AMG 510 in patients with NSCLC were digitized.<sup>7</sup> Tumor responses from patients

treated with 180 ( $n = 3$ ), 360 ( $n = 1$ ), and 720 mg ( $n = 5$ ) were statistically indistinguishable from 960 mg ( $n = 13$ ) distribution (Table S2), hence the multiple-dose data was compiled for generating the virtual population. We assumed protein bound fraction of AMG 510 was the same as that measured for ASP2453 ( $f_b = 0.9926$ ), and a virtual cohort ( $n = 1000$ ) was generated by simulating the AMG 510 clinical protocol and randomizing  $\mu_{max}$  and  $\delta_{max}$  by Monte-Carlo sampling from a log-normal distribution (Figure S1). A virtual population ( $n = 200$ ) was then generated by PW approach,<sup>18</sup> such that the simulated changes in tumor size at 6 weeks matched the published distribution, and growth of untreated tumors was consistent with published data ( $-10$  to  $300\%$  change<sup>17</sup>; Figure 6b, Table 3). The model thus now links AMG 510-mediated KRAS-inhibition, via cellular signaling cascades, to population-level tumor growth.

## Virtual clinical trials for ASP2453 and AMG 510

PK/PD profiles of ASP2453 vs. AMG 510 (dosed 10 through 1280 mg q.d.) were simulated using the drug-specific  $k_{on}$  and projected PK parameters (Figure 6c). Although predicted exposure in ASP2453 was much lower due to the larger volume of distribution (Table 2), predicted KRAS-GTP inhibition is still greater due to the  $\sim 50$ -fold increased affinity of ASP2453. Consistent with the in vivo xenograft data, inhibition of p-ERK and p-S6 is reduced over time due to the activation of feedback circuits, with p-ERK overshooting baseline levels following  $\sim 1$  week of treatment. NSCLC virtual population tumor responses at 6 weeks to increasing doses of ASP2453 versus AMG 510 are shown in Figure 6d.

To directly compare clinical predictions between ASP2453 and AMG 510, dose-response simulations of RAS-GTP at end of treatment and ORR ( $>30\%$  tumor size reduction) between the two compounds are summarized

**TABLE 3** Virtual cohort and population distributions

Tumor size bins	<i>N</i> (data)	Fz (data)	Fz (V cohort)	Fz (V Pop)
1–1.2	5	0.227	0.335	0.228
0.7–1	6	0.272	0.377	0.272
0.5–0.7	6	0.272	0.151	0.256
0.3–0.5	3	0.136	0.118	0.160
0–0.3	2	0.091	0.019	0.084

*Note.* Tumor size changes following six weeks treatment with AMG 510 at 960 mg q.d.<sup>7</sup> Columns represent the number of patients in each bin from the data (*N*) and the corresponding frequency (Fz), and the frequency of virtual patients falling into each bin for the virtual cohort (V cohort), and virtual population (V Pop).

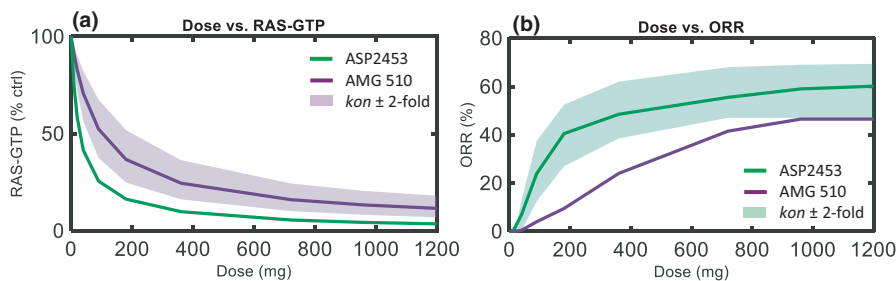


**FIGURE 7** Virtual population mean dose-response projections for AMG 510 versus ASP2453. Virtual population simulations were used to calculate (a) relative RAS-GTP inhibition at 6 weeks post-treatment and (b) overall response rates (ORR; >30% reduction in tumor size at 6 weeks). Uncertainty in  $k_{on}$  estimation for AMG 510 (2-fold around estimate of  $12 \times 10^3 \text{ M}^{-1} \text{ s}^{-1}$ ) is projected via shaded area on the AMG 510 KRAS-GTP and resultant uncertainty on the ASP2453 ORR dose-responses

in Figure 7a and b. Uncertainty in the estimate of  $k_{on}$  for AMG 510 from the in vitro (p-ERK) data was projected to the clinical dose-responses by creating three virtual populations with  $k_{on}$  at the median, lower, and upper bounds of the estimated value ( $6$  to  $24 \times 10^3 \text{ M}^{-1} \text{ s}^{-1}$ , represented by shaded areas in the plots). The 50-fold greater affinity of ASP2453 results in increased KRAS-GTP suppression and higher response rate at equivalent doses (i.e., the 50% ORR reported from AMG 510 at 960 mg is achieved with 380 mg ASP2453).

We can thus use the model to predict how differences in target association rate and PK project to clinical responses for other  $KRAS^{G12C}$  inhibitors where these values are known or predicted.

## DISCUSSION

Predicting clinical outcomes from preclinical data is one of the most challenging tasks in the drug discovery and development process due to a large physiological gap between animals and humans. Here, we have developed a QSP model in NSCLC by integrating two mechanism-based models, one describing RAS-GTP/GDP cycling and inhibitor binding,<sup>13</sup> and one linking cellular signal transduction from RAS, through the MAPK and PI3K pathways, to tumor growth.<sup>12</sup> The model was parameterized using in vitro data, in vivo xenograft PK, PD and tumor growth data, and clinical PK and tumor response data published for AMG 510.<sup>7</sup> The model successfully reproduced the complex PK/PD dynamics in xenograft mice caused by multiple feedback mechanisms within the MAPK pathway. The virtual clinical trial simulations in patients with NSCLC suggested superior clinical efficacy in ASP2453 over AMG 510.

PK/PD modeling has traditionally been applied to predict clinical tumor response of anticancer agents. However, conventional PK/PD models are data-driven and include only limited biological information, hence, clinical translation from animals to humans is typically carried out in an empirical manner.<sup>24,25</sup> In contrast, a QSP model physiologically

describes a biological system and its response to therapeutics.<sup>9,26</sup> Because model components and reactions have biological meaning, a QSP model is capable of addressing more advanced research questions and interpreting complex, non-intuitive data.

Signaling dynamics in response to kinase inhibitor treatments are a prime example. In NCI-H1373 xenograft-bearing mice, the degree of p-ERK and p-S6 inhibition in tumors were decreased after multiple dosing of ASP2453. This phenomenon is hypothesized to be caused by multiple negative feedback loops known to exist within the MAPK pathway.<sup>11,14,15</sup> To verify this, four feedback circuits mediated by DUSP, SPRY, and cMYC, as well as via pathway from AKT to cRAF were incorporated to the model to fit the observed mouse PD data. The model successfully captured the PD behavior in xenografts, indicating contribution of these feedback mechanisms to the observed resistance of p-ERK and p-S6 suppression at steady-state (Figure 3). QSP models thus can be used as a hypothesis testing tool and support quantitative understanding of complex preclinical data.

We also utilized the QSP model to compare the expected clinical response between ASP2453 and AMG 510. The in vitro p-ERK dose-response data in  $KRAS^{G12C}$ -mutant cell lines indicated that the target affinity of ASP2453 was  $\sim 50$ -fold higher than that of AMG 510 (Figure 5a). However, drug efficacy is determined by multiple aspects, not only drug potency but also PK, target tissue distribution, and protein binding. Direct comparison of the anticipated clinical response of a developing compound versus competitors is therefore challenging. In fact, for ASP2453, because plasma exposure was expected to be lower due to the large distribution volume observed in animals, the question of whether this compound would exhibit superior clinical efficacy had been of great concern. To address this question, relevant preclinical data as well as clinical information for AMG 510 were integrated using the model and virtual clinical trial simulations were conducted in patients with NSCLC. The simulations predicted that despite lower exposure, ASP2453 will achieve increased KRAS-GTP suppression and greater ORR at equivalent doses (Figure 7). This result strongly

suggests the potential of ASP2453 to be the best-in-class compound among  $KRAS^{G12C}$  inhibitors and provides confidence on an advancement of ASP2453 to clinical trials.

A couple of assumptions were included in the model due to the lack of available data at the time of model development. First, we assume that the fraction protein bound ( $f_b$ ) of AMG 510 is equivalent to that of ASP2453. Second, we assume that tumor penetration rates ( $k_{12}$  and  $k_{21}$ ) estimated for ASP2453 in NCI-H1373 xenografts holds for both compounds clinically. Exploration of these parameters, however, reveal that changing the either of these assumptions  $\pm 2$ -fold had limited effect of dose versus ORR simulations for ASP2453 (Figure S6). As additional data are released, these parameters can be updated in the model and predictions fine-tuned accordingly. Similarly, as additional clinical data are released, the virtual population can be updated along with clinical predictions.

Additionally, a number of simplifying biological assumptions were made during model development. First, the PI3K/AKT pathway is highly simplified and represents more of a place-holder for non-MAPK dependent proliferative pathways. This was necessary both based on known molecular biology of RAS<sup>3</sup> and the observation that KRAS-inhibition holds sustained activity despite MAPK/ERK signals becoming insensitive over time due to the activation of negative feedback circuits.<sup>27</sup> As such, we do not expect the model to quantitatively predict the effect of combining KRAS-inhibition with PI3K/AKT-targeted therapies (despite predicting generic combination effects with such agents<sup>28</sup>). Second, only cell proliferation and death rates ( $\mu_{max}$  and  $\delta_{max}$ ) were varied to create the virtual cohort and successive virtual populations. Although these are the most sensitive model parameters controlling tumor size, and the approach adequately captured heterogeneity observed both across xenograft models and between patients, likely other molecular model parameters will also vary between tumors (i.e., protein expression levels and basal signaling activity). As such, variability in patient response to inhibitors of these species (i.e., EGFR or PI3K-targeted therapies) are not accounted for, and we thereby also do not expect the virtual population to quantitatively predict the effect of targeted combination therapies. The virtual population could be parameterized to do so, if single agent activity of such compounds was available for the same indication ( $KRAS^{G12C}$ -mutant NSCLC). Finally, the model only explicitly considers tumor cell-autonomous effects of KRAS-inhibition, disregarding the role of the tumor microenvironment and immune system. The adaptive immune response is reported to play a role in the activity of KRAS inhibition,<sup>16,29</sup> as with essentially all cancer therapies.<sup>30</sup> Although these effects are implicitly accounted for in the virtual population, the model in its present formulation will not predict combination effects of immune check-point

blockade, as is planned for the clinical development of these compounds.<sup>6</sup> Despite these limitations, the QSP model and approach in general may serve as a useful drug development tool, representing the first computational model linking molecular properties of a drug class to clinical activity based on a mechanistic description of the cell biology.

In summary, this paper illustrates the successful application of QSP modeling in drug development. The model was applied to the translational prediction of clinical responses, projecting ASP2453 to exhibit greater potency than AMG 510 in patients with NSCLC. The simulation results present potential differentiating features of ASP2453 from its competitor and support critical thinking for clinical trials.

## ACKNOWLEDGEMENTS

The authors would like to sincerely thank Ms. Ayako Nakayama, Mr. Yoshihiro Nishizono, and Mr. Yosuke Yamanaka for conducting experiments. We are also grateful to Drs. Helen Moore and Kota Toshimoto for useful discussions and suggestions on mathematical models and Dr. Jennifer Park for her support in initiating the collaboration.

## CONFLICT OF INTEREST

H.S., T.N., T.M., and Y.N. are employees of Astellas Pharma Inc. M.S. is an employee of Astellas Research Institute of America LLC. D.M., J.F.A., J.M.B., L.W., and D.C.K. were employees of Applied BioMath LLC when this work was conducted.

## AUTHOR CONTRIBUTIONS

D.K., H.S., T.N., M.S., T.M., Y.N., and L.W. wrote the manuscript. D.K., D.M., L.W., J.F.A., J.M.B., H.S., T.N., M.S., and T.M. designed the research. D.K., D.M., L.W., and T.N. performed the research. D.K., D.M., and L.W. analyzed the data.

## REFERENCES

1. Seton-Rogers S. KRAS-G12C in the crosshairs. *Nat Rev Cancer*. 2020;20:3.
2. Nacchio M, Sgariglia R, Gristina V, et al. KRAS mutations testing in non-small cell lung cancer: the role of Liquid biopsy in the basal setting. *J Thorac Dis*. 2020;12:3836-3843.
3. Sheridan C. Grail of RAS cancer drugs within reach. *Nat Biotechnol*. 2020;38:6-8.
4. Ostrem JM, Peters U, Sos ML, Wells JA, Shokat KM. K-Ras(G12C) inhibitors allosterically control GTP affinity and effector interactions. *Nature*. 2013;503:548-551.
5. Hong DS, Fakih MG, Strickler JH, et al. KRAS<sup>G12C</sup> Inhibition with Sotorasib in advanced solid tumors. *N Engl Med*. 2020;383:1207-1217.
6. Mullard A. Cracking KRAS. *Nat Rev Drug Discov*. 2019;18:887-891.
7. Govindan R, Fakih MG, Price TJ, et al. Phase I study of AMG 510, a novel molecule targeting KRAS G12C mutant solid tumors. *Ann Oncol*. 2019;30(suppl 5):v163-v164.

8. Jänne PA, Papadopoulos K, Ou I, Rybkin I, Johnson M. A phase 1 clinical trial evaluating the pharmacokinetics (PK), safety, and clinical activity of MRTX849, a mutant-selective small molecule KRAS G12C inhibitor, in advanced solid tumors. In AACR-NCI-EORTC Int. Conf. Mol. Targets. 2019.
9. van der Graaf PH, Benson N. Systems pharmacology: bridging systems biology and pharmacokinetics-pharmacodynamics (PKPD) in drug discovery and development. *Pharm Res.* 2011;28:1460-1464.
10. Zineh I. Quantitative systems pharmacology: a regulatory perspective on translation. *CPT Pharmacometrics Syst Pharmacol.* 2019;8:336-339.
11. Sturm OE, Orton R, Grindlay J, et al. The mammalian MAPK/ERK pathway exhibits properties of a negative feedback amplifier. *Sci Signal.* 2010;3:ra90.
12. Kirouac DC, Schaefer G, Chan J, et al. Clinical responses to ERK inhibition in *BRAF*<sup>V600E</sup>-mutant colorectal cancer predicted using a computational model. *NPJ Syst Biol Appl.* 2017;3:14.
13. Stites EC, Shaw AS. Quantitative systems pharmacology analysis of KRAS G12C covalent inhibitors. *CPT Pharmacometrics Syst Pharmacol.* 2018;7:342-351.
14. Moelling K, Schad K, Bosse M, Zimmermann S, Schweneker M. Regulation of Raf-Akt cross-talk. *J Biol Chem.* 2002;277:31099-31106.
15. Chen WW, Schoeberl B, Jasper PJ, et al. Input-output behavior of ErbB signaling pathways as revealed by a mass action model trained against dynamic data. *Mol Syst Biol.* 2009;5:239.
16. Canon J, Rex K, Saiki AY, et al. The clinical KRAS(G12C) inhibitor AMG 510 drives anti-tumour immunity. *Nature.* 2019;575:217-223.
17. Infante M, Berghmans T, Heuvelmans MA, Hillerdal G, Oudkerk M. Slow-growing lung cancer as an emerging entity: from screening to clinical management. *Eur Respir J.* 2013;42:1706-1722.
18. Allen RJ, Rieger TR, Musante CJ. Efficient generation and selection of virtual populations in quantitative systems pharmacology models. *CPT Pharmacometrics Syst Pharmacol.* 2016;5:140-146.
19. Gadkar K, Kirouac DC, Mager DE, van der Graaf PH, Ramanujan S. A six-stage workflow for robust application of systems pharmacology. *CPT Pharmacometrics Syst. Pharmacol.* 2016;5:235-249.
20. Strelow JM. A perspective on the kinetics of covalent and irreversible inhibition. *SLAS Discov.* 2017;22:3-20.
21. Janes MR, Zhang J, Li L-S, et al. Targeting KRAS mutant cancers with a covalent G12C-specific inhibitor. *Cell.* 2018;172:578-589.
22. Hallin J, Engstrom LD, Hargis L, et al. The KRAS<sup>G12C</sup> inhibitor MRTX849 provides insight toward therapeutic susceptibility of KRAS-mutant cancers in mouse models and patients. *Cancer Discov.* 2020;10:54-71.
23. Molina-Arcas M, Moore C, Rana S, et al. Development of combination therapies to maximize the impact of KRAS-G12C inhibitors in lung cancer. *Sci Transl Med.* 2019;11:eaaw7999.
24. Gu Y, Sai Y, Wang J, et al. Preclinical pharmacokinetics, disposition, and translational pharmacokinetic/pharmacodynamic modeling of savolitinib, a novel selective cMet inhibitor. *Eur J Pharm Sci.* 2019;136:104938.
25. Titze MI, Schaaf O, Hofmann MH, et al. An allometric pharmacokinetic/pharmacodynamics model for BI 893923, a novel IGF-1 receptor inhibitor. *Cancer Chemother Pharmacol.* 2017;79:545-558.
26. van der Vicini P, Graaf PH. Systems pharmacology for drug discovery and development: paradigm shift or flash in the pan? *Clin Pharmacol Ther.* 2013;93:379-381.
27. Samatar AA, Poulidakos PI. Targeting RAS-ERK signalling in cancer: promises and challenges. *Nat Rev Drug Discov.* 2014;13:928-942.
28. Misale S, Fothergill JP, Cortez E, et al. KRAS G12C NSCLC models are sensitive to direct targeting of KRAS in combination with PI3K inhibition. *Clin Cancer Res.* 2019;25:796-807.
29. Tape C, Ling S, Dimitriadis M, et al. Oncogenic KRAS regulates tumor cell signaling via stromal reciprocation. *Cell.* 2016;165:910-920.
30. Chen DS, Mellman I. Elements of cancer immunity and the cancer-immune set point. *Nature.* 2017;541:321-330.
31. Mageean CJ, Griffiths JR, Smith DL, Clague MJ, Prior IA. Absolute quantification of endogenous ras isoform abundance. *PLoS One.* 2015;10:e0142674.
32. Sunaga N, Shames DS, Girard L, et al. Knockdown of oncogenic KRAS in non-small cell lung cancers suppresses tumor growth and sensitizes tumor cells to targeted therapy. *Mol Cancer Ther.* 2011;10:336-346.
33. Shukla S, Sankar Allam U, Ahsan A, et al. KRAS protein stability is regulated through SMURF2: UBCHE5 complex-mediated  $\beta$ -TrCP1 degradation. *Neoplasia.* 2014;16:115-128.
34. Patricelli MP, Janes MR, Li L-S, et al. Selective inhibition of oncogenic KRAS output with small molecules targeting the inactive state. *Cancer Discov.* 2016;6:316-329.

## SUPPORTING INFORMATION

Additional supporting information may be found online in the Supporting Information section.

**How to cite this article:** Sayama H, Marcantonio D, Nagashima T, et al. Virtual clinical trial simulations for a novel KRAS<sup>G12C</sup> inhibitor (ASP2453) in non-small cell lung cancer. *CPT Pharmacometrics Syst Pharmacol.* 2021;10:864–877. <https://doi.org/10.1002/psp4.12661>